

Tethered balloon-based black carbon profiles within the lower troposphere of Shanghai in the 2013 East China smog



Juan Li^a, Qingyan Fu^{a,*}, Juntao Huo^a, Dongfang Wang^a, Wen Yang^b, Qinggen Bian^a, Yusen Duan^a, Yihua Zhang^a, Jun Pan^a, Yanfen Lin^a, Kan Huang^{c,**}, Zhipeng Bai^f, Sheng-Hsiang Wang^d, Joshua S. Fu^c, Peter K.K. Louie^e

^a Shanghai Environmental Monitoring Center, Shanghai, 200030, China

^b Chinese Research Academy of Environmental Sciences, Beijing, 100012, China

^c Department of Civil and Environmental Engineering, The University of Tennessee, Knoxville, TN 37996, USA

^d Department of Atmospheric Sciences, National Central University, Chung-Li, Taiwan

^e Hong Kong Environmental Protection Department, Hong Kong, China

^f State Key Laboratory of Environmental Criteria and Risk Assessment, Atmospheric chemistry & Aerosol Division, Chinese Research Academy of Environmental Sciences, Beijing 100012, China

HIGHLIGHTS

- A Tethered balloon-based black carbon measurement was firstly conducted in a megacity of China.
- Diurnal characteristics, formation, and sources of black carbon profiles were revealed.
- High atmospheric heating effects due to black carbon may influence regional climate.

ARTICLE INFO

Article history:

Received 2 March 2015

Received in revised form

13 July 2015

Accepted 31 August 2015

Available online 2 September 2015

Keywords:

Black carbon

Vertical profile

Tethered balloon

Haze

Shanghai

ABSTRACT

A Tethered balloon-based field campaign was launched for the vertical observation of air pollutants within the lower troposphere of 1000 m for the first time over a Chinese megacity, Shanghai in December of 2013. A custom-designed instrumentation platform for tethered balloon observation and ground-based observation synchronously operated for the measurement of same meteorological parameters and typical air pollutants. One episodic event (December 13) was selected with specific focus on particulate black carbon, a short-lived climate forcer with strong warming effect. Diurnal variation of the mixing layer height showed very shallow boundary of less than 300 m in early morning and night due to nocturnal inversion while extended boundary of more than 1000 m from noon to afternoon. Wind profiles showed relatively stagnant synoptic condition in the morning, frequent shifts between upward and downward motion at noon and in the afternoon, and dominant downward motion with sea breeze in the evening. Characteristics of black carbon vertical profiles during four different periods of a day were analyzed and compared. In the morning, surface BC concentration averaged as high as 20 $\mu\text{g}/\text{m}^3$ due to intense traffic emissions from the morning rush hours and unfavorable meteorological conditions. A strong gradient of BC concentrations with altitude was observed from the ground to the top of boundary layer at around 250–370 m. BC gradients turned much smaller above the boundary layer. BC profiles measured during noon and afternoon were the least dependent on heights. The largely extended boundary layer with strong vertical convection was responsible for a well mixing of BC particles in the whole measured column. BC profiles were similar between the early-evening and late-evening phases. The lower troposphere was divided into two stratified air layers with contrasted BC vertical distributions. Profiles at night showed strong gradients from the relatively high surface concentrations to low concentrations near the top of the boundary layer around 200 m. Above the boundary layer, BC increased with altitudes and reached a maximum at the top of 1000 m. Prevailing sea breeze within the boundary layer was mainly responsible for the quick cleanup of BC in the lower altitudes. In contrast, continental outflow via regional transport was the major cause of the enhanced BC aloft. This study provides a first

* Corresponding author.

** Corresponding author.

E-mail addresses: qingyanf@semc.gov.cn (Q. Fu), khuang7@utk.edu (K. Huang).

insight of the black carbon vertical profiles over Eastern China, which will have significant implications for narrowing the gaps between the source emissions and observations as well as improving estimations of BC radiative forcing and regional climate.

© 2015 Elsevier Ltd. All rights reserved.

1. Introduction

Owing to the strong economic development for the last few decades, China has been suffering from serious air pollution problems (Chan and Yao, 2008; Hao et al., 2007; Ouyang, 2013). The significance of trans-boundary transport of pollutants from East Asia, especially China has been extensively reported (Hand, 2014; Park et al., 2004; Yamazaki et al., 2014). For instance, it was reported that one O₃ pollution episode that occurred in Central California during 2012 was ascribed to be related to the long-range transport from China (Hand, 2014). Domestically in China, there have been urgent needs to mitigate air pollution, for it has become a big concern in economics (Lin et al., 2014), agriculture (Liu et al., 2013; Tai et al., 2014), transportation, public health (D'Amato et al., 2013; Kan et al., 2012; Tagaris et al., 2009), and climate change (Jacob and Winner, 2009).

In this regard, the Chinese government has made concerted efforts to tackle air pollution problems in recent years. For example, more rigorous national standard of air quality was promulgated and enforced in August 2013. Shortly after that, the State Council of China issued the Air Pollution Prevention and Control Action Plan. In April 2014, the environmental law was amended for better addressing the current status of air quality in China. Meanwhile, a comprehensive ground-based ambient air quality network for monitoring gaseous pollutants and particulate matters has been established in around 200 cities of the whole country so as to gain a better representation of the levels and spatial patterns of regional air pollution.

Two notorious large scale smog events hovered over North China in early January of 2013 and over East China in December of the same year (Wang et al., 2014; Xu et al., 2013). During these extreme air pollution events, hourly PM_{2.5} concentration on Jan 12 recorded more than 900 µg/m³ in Beijing; and the peak hourly PM_{2.5} concentration on December 6 reached 602 µg/m³ in Shanghai, 7–8 times higher than the national 24-h standard of 75 µg/m³. High emissions, rapid formation of secondary aerosols and strong regional transport under the stagnant weather condition were investigated to be the major factors for the formation of these extreme haze events (Ji et al., 2014). However, most of the previous studies mainly focused on the characteristics of air pollutants on the surface level. Little has been known on the vertical variation of air pollutants in the lower troposphere; How would the variation of atmospheric boundary layer control the vertical mixing extent; And what's the impact of regional transport on the perturbation of air pollutants' vertical distributions.

Currently, the most widely applied instrumentations in the field measurement of vertical observation for airborne pollutants include aircraft, kite, tower, and the Tethered balloon platform. For aircraft based measurement, it was mainly focused on the mid- and high-altitudes of around 1–10 km (Ding et al., 2009; Yerramilli et al., 2008), but the vertical resolution is relatively low. Aircraft was used to carry on canisters sampling for the volatile organic compounds (Winkler et al., 2002). For a kite, it can be operated at a height as low as 100 m (Knapp et al., 1998), but the light-weight payload is the shortcoming for this platform. As

for a tower, it is set up at a fixed site and also has limited observation range depending on the height of the tower. For example, in Beijing, there is a 325 m tower deployed for the measurement of meteorological and air pollutants fields (Meng et al., 2008). The well-known Eiffel tower in Paris was also used to collect observation data (Dupont et al., 1999). Measurements on the Frohnau Tower in Berlin were conducted to explore the cause of elevated PAN and O₃ (Rappengluck et al., 2004). As for a Tethered balloon, in theory it can be launched at any locations even in the harsh environment such as the South pole (Johnson et al., 2008) as well as in cities (Greenberg et al., 2009; Lin et al., 2007; Ma et al., 2013; Day et al., 2010; Cuchiara et al., 2014). Its application could be traced back to 1990's (Baumbach et al., 1993). However, the traditional Tethered balloon platform was also limited with the payload and generally could only carry the light-weight instruments.

In this study, we used a Tethered balloon to investigate the atmospheric chemistry in the lower troposphere, especially within the atmospheric boundary layer, in a metropolitan Chinese city, Shanghai. A custom-designed Tethered balloon filled with 1600 m³ Helium with the payload capacity of 200 kg was used. This study is believed to be the first vertical airborne observation within the 1000 m troposphere over a metropolitan area in China. Particulate black carbon (BC) is the primary aerosol species investigated in this study. Although it only accounted for 5–10% of the aerosol mass in cities of China (Ni et al., 2012; Zhang et al., 2012), BC plays a significant role in the visibility degradation (Zhang et al., 2012), adverse health effect (Smith et al., 2009), and regional climate warming (Ramanathan and Carmichael, 2008). Its predominant sources are combustion related, e.g. fossil fuels consumption from transportation, industries, and residential usage, and open burning of biomass. Since BC is a relatively inert species, it could be regarded as a good tracer to probe the potential emission source region and the transport behavior of plumes at a specific receptor site. Most of the studies on the vertical distribution of black carbon focused on the altitudes of ~10 km with the vertical resolution of 0.5–1.0 km using aircrafts to explore the climate effect induced by BC (Babu et al., 2011; Rahul et al., 2014; Ramana et al., 2010; Xue et al., 2010). In Shanghai, very few studies on the vertical distribution of air pollutants were conducted. Geng et al. (2009) explored the vertical distribution of SO₂, O₃, VOC and NO_x within 15 km in late-September and early-October over the Yangtze River Delta by means of an aircraft and suggested future traffic emissions will be responsible for the enhancement of O₃ pollution.

As a pilot study of the vertical observation of BC, we aim to explore the characteristics of BC profiles within the 1000 m lower troposphere over a Chinese megacity. BC profiles sampled during different time frames in a day were compared. The impact of varying meteorological conditions and boundary layer on shaping the BC vertical profiles was specifically assessed. The field experiment conducted in this study not only advances the atmospheric observational technology above the ground level, but also shed light on the nature and causes of heavy air pollution in China. It may also improve the performance and forecast accuracy of air quality models at the regional scale.

2. Methodology

2.1. Field measurement

In December of 2013, one intensive field campaign equipped with Tethered balloon was launched in Shanghai, which is located in the Yangtze River Delta in East China. The field measurement site ($30^{\circ}49'47''$ N, $121^{\circ}30'04''$ E) was set up in a rural area at the southern edge of Shanghai in the Fengxian District as shown in Fig. 1. The surrounding area is mainly occupied by a number of university campuses and there is a chemical industrial park around 10 km southwest from this field. This site is located to the south of downtown Shanghai and is about 45 km away. During winter of this study, the prevailing winds are from the north. Hence, this site could be regarded as a good receptor from urban emissions. This monitoring site is ~47 km from the Hongqiao Airport and ~42 km from the Pudong Airport, respectively. As shown in Fig. 1, this monitoring site is an ideal location away from both airports as far as possible. During the field campaign, strict coordination with the air force was mandatory to make sure that all tether-balloon measurements were launched without any aviation activities nearby the monitoring site for safety issues. Hence, the impacts from aviation emissions could be regarded negligible.

2.1.1. Description of the tethered balloon platform

The tethered balloon platform consisted of two major components. The jet-shape Tethered balloon acted as the carrier filled with 1600 m^3 Helium gas; a rack was self-designed to deploy all the monitoring instruments with the size of $1240\text{ mm} \times 1825\text{ mm} \times 650\text{ mm}$. This assembly was firmly mounted underneath the Tethered balloon as shown in Fig. 2a&b. A Tethered line is connected to the balloon to provide electricity for all the instruments and telecommunication between ground and the balloon. The design of the balloon allows a maximum payload of 200 kg. The monitoring instrument assembly was deployed to measure the height and location of the balloon (GPS, Model: HC12), meteorological parameters (Temperature–Humidity sensor, Model: MT-EC-8SX), and black carbon (Aethalometer, Model: AE31). The meteorology sensor was mounted on the nose of the Tethered balloon.

In this study, the Tethered balloon platform was used for the profile measurement. The balloon was launched to ascend at a steady speed of 0.5 m/s till a maximum height of 1000 m. It remained at the height of 1000 m for 5 min, and then descended with the same rate. Based on the recorded flow rates of the instrument during the operation, we have verified that this speed would not impact on the designed flow rates of the deployed instruments. The experiments were conducted when the ground wind speeds were lower than 5 m/s without significant precipitation. All of observed real-time data were transmitted at the interval of 10 s through an optical transceiver to the developed information system as the platform operated. In a given day, the Tethered balloon was scheduled to be launched during four time periods around sunrise, noon, sunset, and midnight, respectively. However, profiles of the four time periods in the same day could not be obtained in some sampling days due to the weather and malfunction of the instruments.

2.1.2. Synchronous ground-based observation

The Tethered balloon measurement was initiated above the height of 150 m. This was due to that the transition of power from the standard (220 V) to high-voltage (1800 V) supply started to function above this height for the safety protection of operators on the ground. To obtain a full picture of the vertical distribution of air pollutants from the ground to the upper levels, all parameters were synchronously measured using the same instruments equipped in a ground monitoring vehicle.

In addition, a Lidar (Model: WindCube70) was set up in the field to measure the wind profiles. Accuracy of wind speed and direction is about 0.3 m/s and 1.5° , respectively. Mixing layer height (MLH) was retrieved by a ceilometer (Model: CL31) synchronously. The method of MLH inversion from ceilometer is based on the profiles of attenuated backscatter where it experienced the steepest gradient (Eresmaa et al., 2006). The overview picture of field campaign is depicted in Fig. 2c.

2.1.3. Quality assurance and quality control

To assure the quality and reliability of the observations, all the deployed instruments were examined thoroughly and flow rates were calibrated before and after the field campaign. Aethalometer

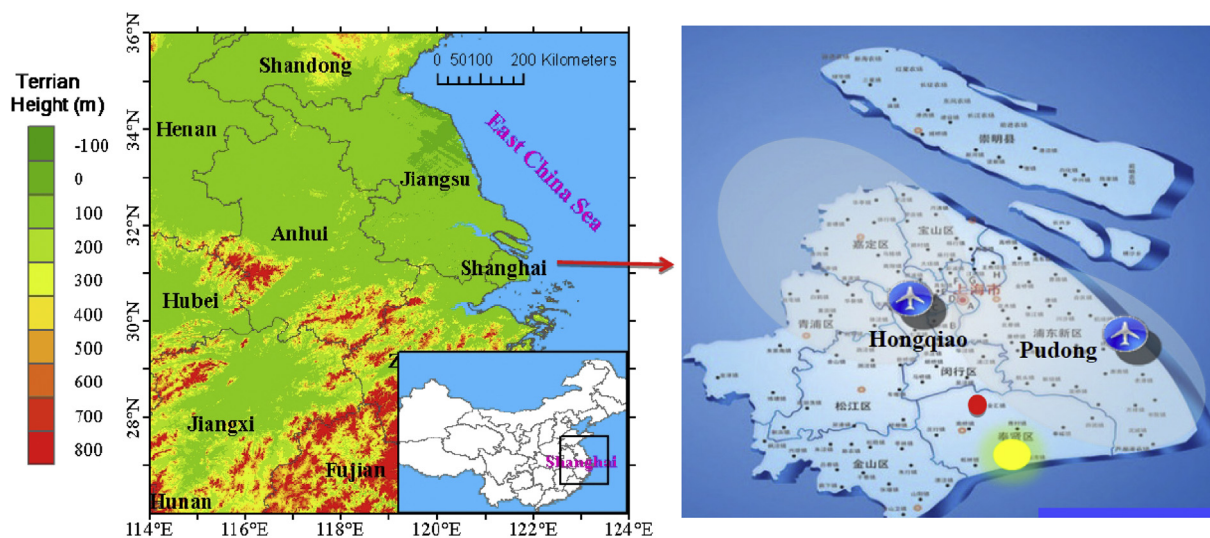


Fig. 1. Location of the field campaign conducted in Shanghai during December, 2013. The yellow dot is the Tethered balloon field campaign site and the red dot represents a ground-based monitoring site operated by SEMC. Locations of the two airports (Hongqiao and Pudong) are also indicated on the map. (For interpretation of the references to colour in this figure legend, the reader is referred to the web version of this article.)

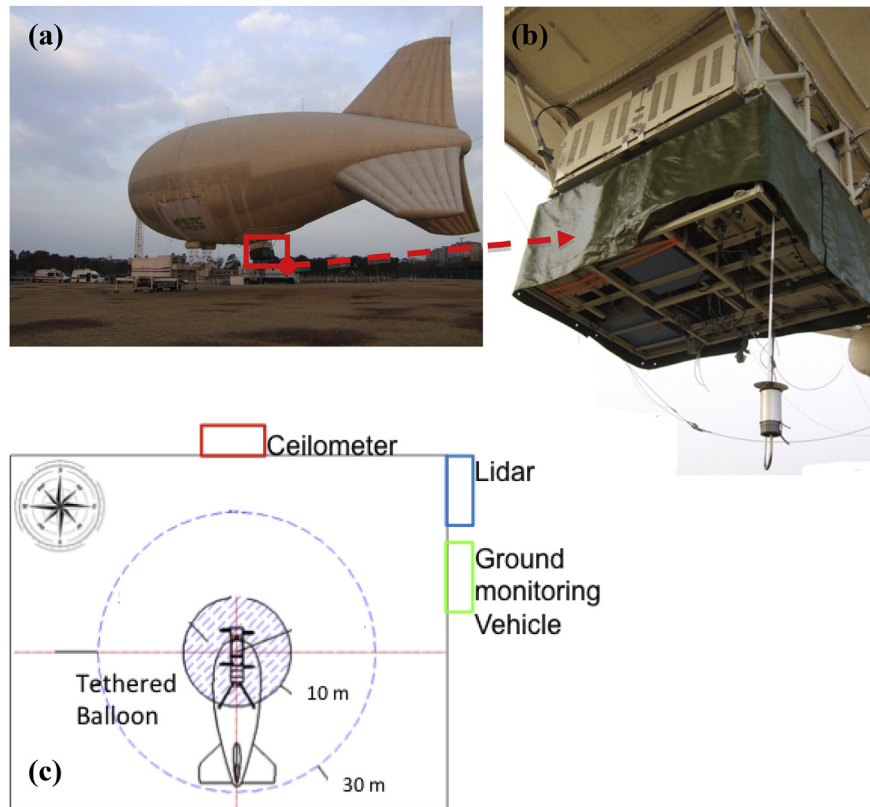


Fig. 2. (a) Picture of the Tethered balloon platform deployed in the field (b) the monitoring instrument assembly attached underneath the Tethered balloon (c) the overview picture of all monitoring equipments deployed in the field.

(AE31, Magee Scientific Co.) was deployed to continuously measure BC concentrations by the means of the attenuated light that transmitted through the samples when collected on a filter. Owing to the known issues of multiple scattering and filter loading problems, the measured aerosol absorption coefficient needs to be corrected and in this study an empirical correction method proposed by [Arnott et al. \(2005\)](#) is used as follows:

$$B_{abs,n} = \frac{SG BC_n - \alpha B_{sca,n}}{M} \sqrt{1 + \frac{\left(\frac{Vdt}{A}\right) \sum_{i=1}^{n-1} B_{abs,i}}{\tau_{afx}}}$$

where n represents the n -th measurement of BC. V is the flow rate, dt is the measurement interval, and A is the filter area. SG , α , M , and τ_{afx} are empirical values that are listed in a lookup table in [Arnott et al. \(2005\)](#). In addition, pairs of instruments for the identical species measured in the upper level and on the ground were compared to make sure there were no obvious systematic errors between each other. In this study, two AE31 aethalometers which were deployed on the balloon platform and on the ground surface were inter-compared before the field campaign. The result is shown in [Fig. 3](#) and a linear regression equation was fit as $BC_b = (1.10 \pm 0.04) BC_m - (-304.0 \pm 57.9)$, $R^2 = 0.99$, $N = 200$, where BC_b and BC_m (units: ng/m^3) denote the instrument that is deployed under the balloon and on the ground, respectively. The results above suggested no systematic errors existed between the two aethalometers.

2.2. Atmospheric heating rates

In this study, the atmospheric heating rates due to black carbon aerosol are estimated by a solar radiative transfer model (CLIRAD-

SW) developed by [Chou and Suarez \(1999\)](#) and [Chou et al. \(2002\)](#). This model considers solar radiation absorption by water vapor, O_3 , O_2 , CO_2 , and Rayleigh scattering, and the absorption and scattering due to aerosols. [Fomin and Correa \(2005\)](#) implemented new parameterizations in CLIRAD-SW and the version used in this study is called CLIRAD (FC05)-SW. Spectrum of aerosol is divided into eight bands from 200 to 10,000 nm in the model. The aerosol input parameters for calculating the radiative heating rates include wavelength dependent AOD, single scattering albedo and asymmetry factor. Wavelength dependent AOD due to black carbon (i.e. AAOD) are calculated by the measured BC profile and the layer height.

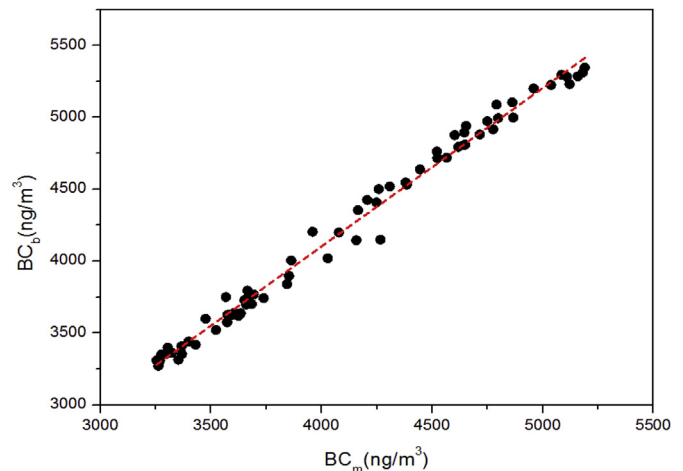


Fig. 3. Comparison of BC concentrations measured by two AE 31 aethalometers, which were used for the balloon observation and the ground observation, respectively.

Single scattering albedo and asymmetry factor of BC are taken from a lookup table in (Wang et al., 2007). The surface albedo for December of 2013 is from the Moderate Resolution Imaging Spectroradiometer (MODIS) 16-day Albedo products (MCD43C3.005). The atmospheric heating rates can be calculated using the equation as below:

$$\frac{\partial T}{\partial t} = \frac{g_a}{c_p} \frac{\Delta F(p)}{\Delta p}$$

Where $\frac{\partial T}{\partial t}$ is the heating rate (K/day), g_a is the acceleration due to gravity, c_p is the specific heat capacity of air at constant pressure ($\sim 1006 \text{ J kg}^{-1} \text{ K}^{-1}$) and $\Delta F(p)$ is the net flux divergence of a pressure layer p .

The atmospheric heating rate (HR_{bc}) due to black carbon is then given by the equation below:

$$HR_{bc} = \frac{\partial T}{\partial t} (\text{with black carbon}) - \frac{\partial T}{\partial t} (\text{without black carbon})$$

3. Results and discussions

3.1. General overview of the December air quality in Shanghai

Winter is the most severe air pollution season in China due to the enhanced emissions and unfavorable meteorological conditions. Fig. 4a shows the daily AQI (Air Quality Index) with different grades from “excellent” to “severely polluted” during the whole December in Shanghai. The average monthly $\text{PM}_{2.5}$ concentration reached $125.2 \mu\text{g}/\text{m}^3$, about 1.7 times of the Chinese National Ambient Air Quality Standards Grade II ($75 \mu\text{g}/\text{m}^3$). In a record breaking heavy haze pollution on December 6, 2013, the hourly maximum $\text{PM}_{2.5}$ concentration reached $602.3 \mu\text{g}/\text{m}^3$. As reported by the daily AQI, only 8 days ($\text{AQI} \leq 100$) were considered as good air quality days. In turn, almost 75% of the days were polluted in different extents. Fig. 4b shows the monthly mean AAOD (Absorption Aerosol Optical Depth), a good indicator of black carbon, retrieved from OMI (Ozone Monitoring Instrument, See Appendix in Supplementary Materials) onboard Aura in December. Hot spots of AAOD that exceeded 0.05 spread over the northeastern China, including most areas of the North China Plain, Central China, as well as the Yangtze River Delta. This implied that Shanghai encountered intense emissions that emitted absorbing aerosols in December 2013. The spatial pattern of AAOD resembled that of BC anthropogenic emissions (Fig. S1). During this Tethered balloon field campaign, we sampled BC profiles for a number of days. The BC profile on December 13, 2013 is chosen to be analyzed in this study as this day includes the most complete profiles sampled during four different periods in a day.

3.2. Synoptic weather conditions on December 13, 2013

3.2.1. Diurnal variation of the mixing layer height

Mixing layer height is a key parameter influencing the vertical dispersion of air pollution via the turbulent mixing (Emeis et al., 2008). The diurnal variation of mixing layer height (MLH) retrieved from the ceilometer on Dec. 13, 2013 is presented in Fig. 5. Prior to LST 11:00, MLH was shallow in the range of 150–540 m. It should be noted that the entrainment of cold front from the north and formation of local mist delayed the development of boundary layer in the morning. As the solar radiation enhanced, the boundary layer rapidly developed and stayed at relatively high values of 1000–1640 m between LST 14:00–18:00. MLH reached its maximum of 1640 m at LST 16:00. Urban heat island effect sustained the high mixing layer even after sunset. However, only after

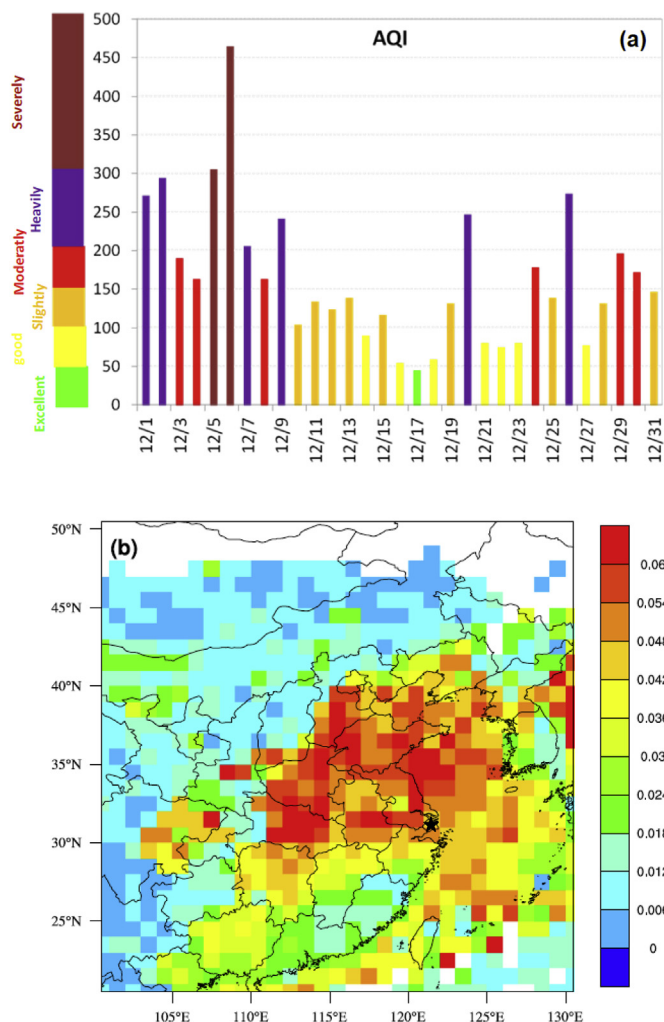


Fig. 4. (a) Daily variation of AQI (Air Quality Index) in December, 2013. Different colors represent different grades of air quality (b) The spatial distribution of monthly mean AAOD (Absorption Aerosol Optical Depth) retrieved from OMI (Ozone Monitoring Instrument) in December, 2013. Location of Shanghai is denoted by the black star on the map. (For interpretation of the references to colour in this figure legend, the reader is referred to the web version of this article.)

a short duration of 3 h, MLH dropped to an extremely low value of 190 m, and remained at low levels in the following hours, indicating poor dispersion conditions during this study period.

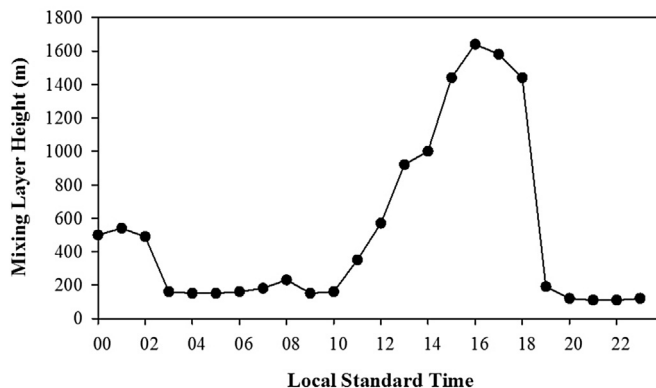


Fig. 5. The diurnal variation of mixing layer height on December 13, 2013 derived from ceilometer.

3.2.2. Diurnal variation of wind profiles

Fig. 6 shows the time–height cross section of wind profile retrieved from the Lidar on December 13, 2013. The duration of Lidar measurement on this day was available from LST 4:46 to 21:42. Fig. 6a refers to the time–height cross section of the vertical components of winds, of which the positive values meant downward air flows while the negative values meant upward air flows. From early morning to LST 10:20, although upward motion was observed, the vertical wind was very weak with the values of 0–0.2 m/s, implying the vertical convection within the lower troposphere was negligible and the synoptic condition was relatively stable. Starting from noon, the upward and downward winds began to take shift as the day progressed. Upward wind speeds slightly strengthened especially at higher altitudes of more than 650 m. The downward wind speeds were evidently higher and could reach 1–2 m/s, implying that the turbulence of the

atmospheric boundary layer was enhanced due to the stronger solar radiation. In the evening from LST 17:00, the upward winds were almost absent. At lower altitudes, the vertical motion was still. Downward winds were predominant especially at higher levels with wind speeds of 0.2–1.0 m/s. The subsidence of air during the evening may transport pollutants from adjacent areas.

As shown in Fig. 6b, horizontally, winds prevailed from north and northeast at all altitudes before noon. Wind speeds below 300 m were 0.8–4.0 m/s higher than the upper levels. As the day progressed, wind speed slowed and winds gradually shifted from the northeast around noon. During LST 13:00–15:00, winds derived from a variety of directions and no prevailing winds were observed. Starting from the afternoon around LST 17:00, more northeasterlies, i.e. sea breeze, were observed at lower levels below 300 m. While at the higher altitudes, winds shifted from the southeast with higher wind speed.

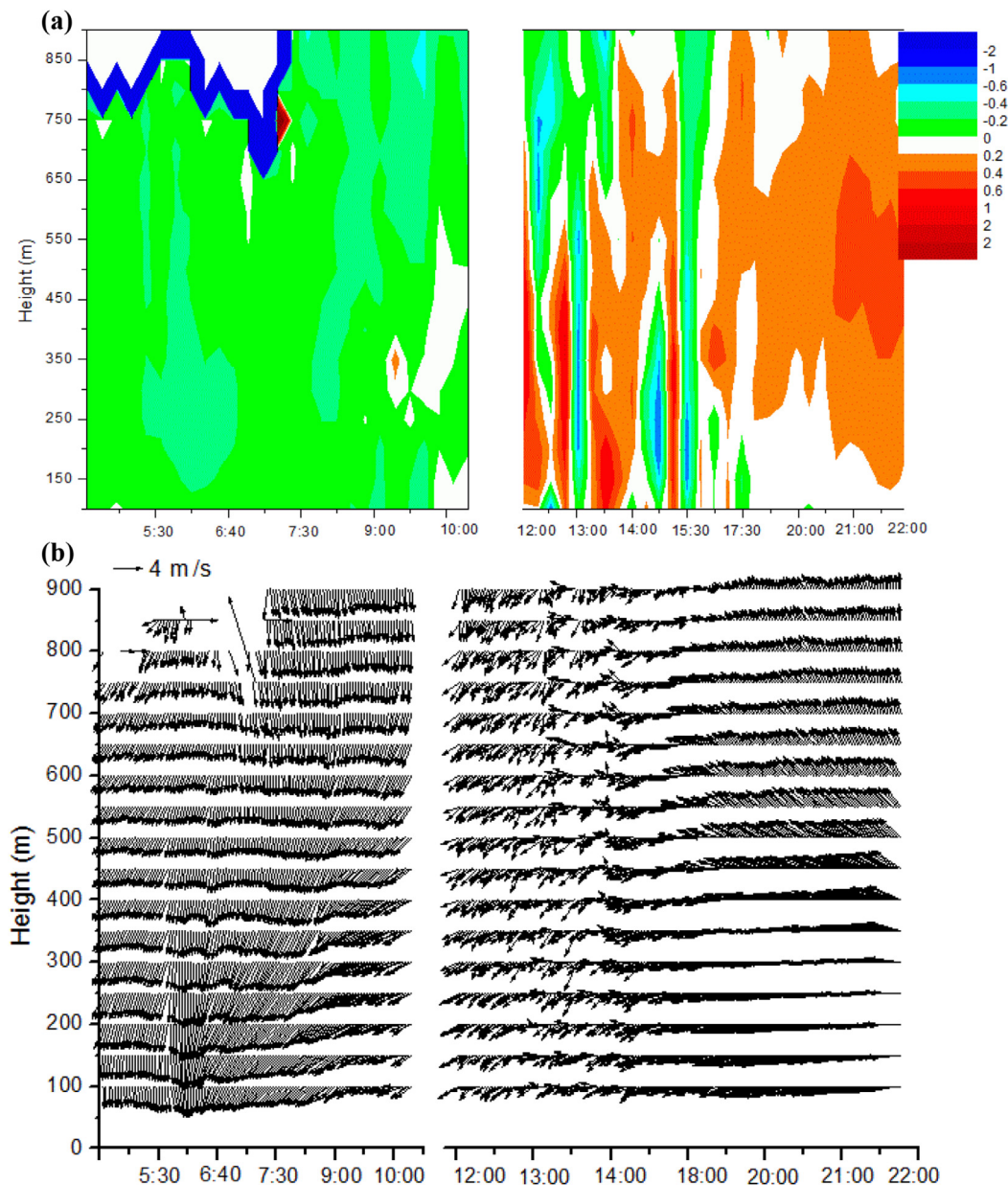


Fig. 6. Time series of wind profile depending on altitudes from LST 4:46 to 21:42 on December 13, 2013. (a) vertical components of wind: a positive value means the downward motion, and vice versa (b) horizontal components of wind.

In comparison, it was clearly seen that horizontal wind speed is more than 10 times higher than the vertical, indicating the horizontal transport should play an important role in shaping the vertical profiles of air pollutants.

3.3. Diurnal variation of BC near the surface

Fig. 7a shows the hourly variation of BC measured at the surface level on Dec. 13, 2013. The mean BC concentrations during morning (4–10 AM), noon and afternoon (10 AM–16 PM), early-evening (16–20 PM), and late-evening (20 PM–00 AM) were 20.0, 5.7, 3.8, and 5.6 $\mu\text{g}/\text{m}^3$, respectively, BC level in the morning was evidently much higher than any other phases. Since BC is the only aerosol chemical species measured at the Tethered balloon site, it is hard to apportion its dominant emission sources on a diurnal scale. Alternatively, we chose another ground-based site operated by SEMC (Shanghai Environmental Monitoring Center) to supplement the source apportionment. As shown in Fig. 1b (red circle), this site is located northwest to the Tethered balloon site and about 15 km from our sampling site. During this study period, the prevailing horizontal winds were from the north and northeast. Hence, the Tethered balloon field site could be regarded as a receptor from the areas where the SEMC site is located. Hourly OC and EC concentrations at the SEMC site are available as shown in Fig. 7b. BC and EC at the two sites showed consistent variations, suggesting the influence from similar emissions. It is noted that the OC/EC ratios reached low values of less than 4.0 during LST 6–8 AM when element carbon showed the highest concentrations. As indicated in Fig. S1, power plants shouldn't be the major source as the contribution was rather low although the OC/EC emission ratio from coal-

fired power plants was in the range of 3–6 based on a comprehensive study of OC and EC source profiles from various sectors (Chow et al., 2011). As for the residential emission, the OC/EC ratio was around 2.7 and 12.7 for coal combustion and natural gas combustion, respectively (Chow et al., 2011). Since winter residential heating is not applied in southern China and coal is not usually used in households of Shanghai, the residential sector shouldn't be the major contributor to the high BC levels in the morning, either. As for the transportation sector, the OC/EC ratio for the gasoline vehicles was around 2–4 while less than 1 for the diesel vehicles (Chow et al., 2011). Hence, the measured OC/EC ratios in the early morning were more close to that from the transportation sector.

Shanghai possessed more than 2.7 million motor vehicles as of 2014 and vehicle emission is one of the major sources of black carbon in Shanghai (Huang et al., 2012). Traffic congestions were ubiquitous during the rush hours in Shanghai, which caused more emissions such as black carbon due to less efficient combustion (Chen et al., 2007). Unfavorable meteorological conditions also contributed to this high level of BC concentrations in addition to the enhanced emissions. As shown in Fig. 5, very shallow boundary layer in the range of 150–230 m could trap most of the emissions and significantly elevated the surface BC concentrations. Fig. 6a shows the morning vertical convection was weak. Besides, the persistent northerlies (Fig. 6b) also likely brought pollutants from downtown Shanghai and the adjacent provinces to the sampling site. Therefore, locally generated emissions (mainly from traffic) plus the regional emissions under the unfavorable meteorological conditions were responsible for the extremely high BC concentrations in the morning.

During the noon and afternoon phase, BC concentration was lowered about 3.5 times on average compared to the morning. Wind direction gradually shifted from northerly land wind to the easterly sea breeze. Along with the significantly reduced traffic flows, BC concentrations were much reduced. Fig. 7b shows elevated OC/EC ratios of more than 4.0 at the SEMC site during the noon and afternoon phase, the highest in this day. Increased industrial emissions should be partially responsible for this as this emission sector was characterized of higher OC/EC ratios. As for the early evening phase, although it encountered the evening rush hours, BC showed the lowest level compared to the other phases. One reason could be that the evening rush hour duration was more extended (from ~16:30 to ~20:30 PM) than the morning rush hour (from ~7 to ~9 AM), thus the emissions were not accumulated in a short period. Another cause should be due to the favorable dispersion condition that the boundary layer further developed during the early evening phase to a maximum of 1640 m at LST 16:00 as indicated by Fig. 5. After the evening rush-hour, the BC level showed moderate increases during the late-evening phase. Since no intense traffic emission was expected and industrial emission was at its minimum, the increase of BC should be mainly related to the sharp decrease of the mixing layer height as shown in Fig. 5.

3.4. BC vertical profiles

A total of 10 BC vertical profiles were obtained on December 13, 2013 (Fig. 8) during four time phases, i.e. morning, noon and afternoon, early-evening, and late evening, respectively. In the following sections, we will illustrate the characteristics of BC profile in each phase.

3.4.1. Morning BC profile

Fig. 8a presents the morning BC profiles obtained at 5:30, 8:00, and 9:00, respectively. At 5:30, BC concentration at the ground level

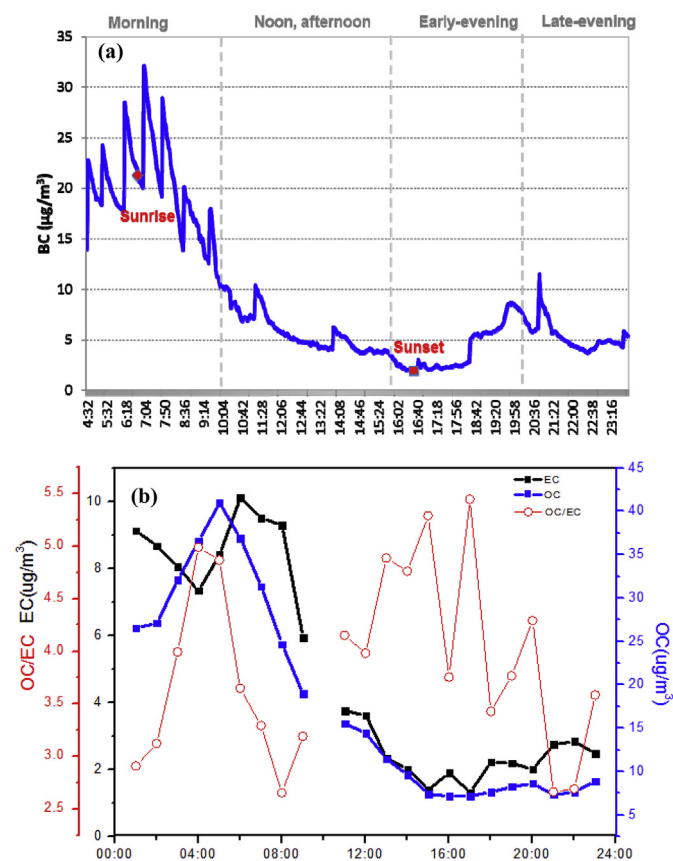


Fig. 7. (a) Time-series of surface BC concentrations measured at the field sampling site on December 13, 2013 (b) Time-series of OC and EC concentrations with the OC/EC ratios measured at the Dianshanhu monitoring site on December 13, 2013.

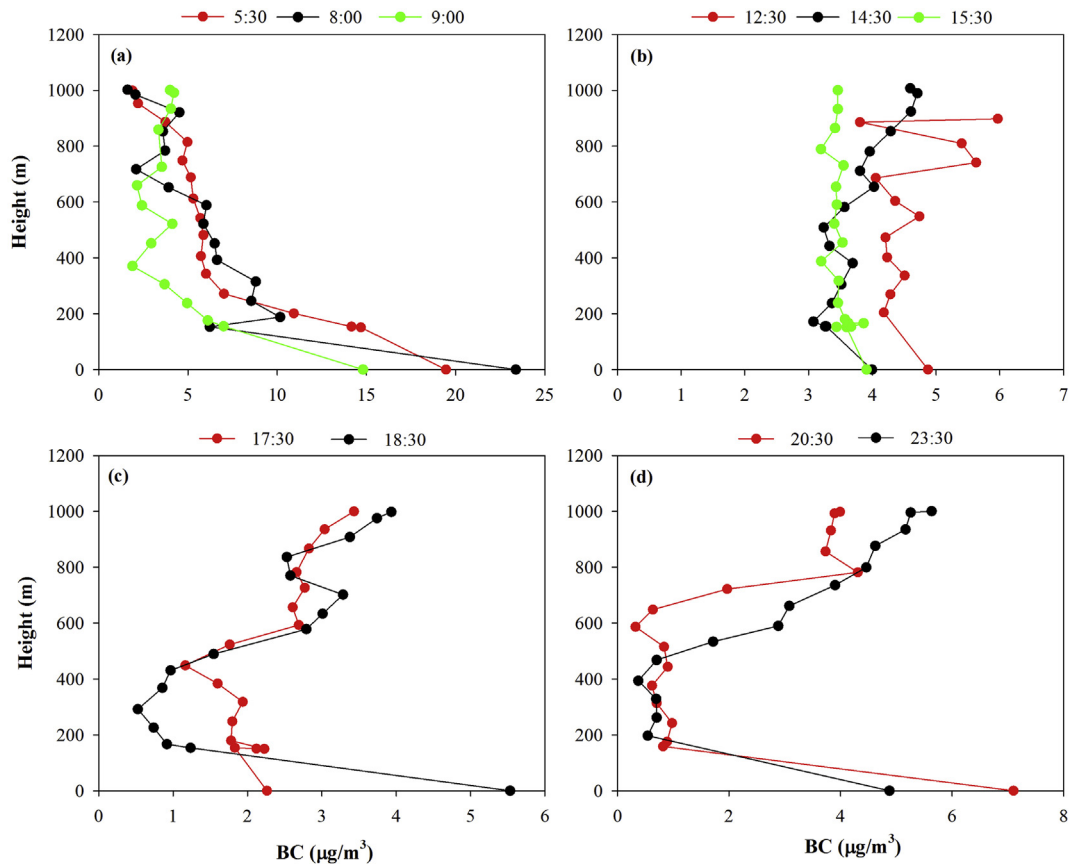


Fig. 8. BC vertical profiles sampled in (a) morning, (b) noon and afternoon, (c) early-evening, and (d) late-evening on Dec. 13, 2013. Note that BC at 0 m represents concentration measured by a ground-based aethalometer; BC concentrations measured by the Tethered balloon started from around 150 m to the top of 1000 m.

reached an extreme high value of $19.5 \mu\text{g}/\text{m}^3$. A strong gradient of BC concentrations with altitude was observed from the ground to $7.0 \mu\text{g}/\text{m}^3$ at 272 m. The decreasing rate from ground to 272 m reached $0.046 \mu\text{g}/\text{m}^3/\text{m}$. Between 272 m and 815 m, the BC gradient was much smaller with the decreasing rate of $0.004 \mu\text{g}/\text{m}^3/\text{m}$. The BC profiles sampled at 8:00 and 9:00 were as similar as that of 5:30 to some extent. At 8:00, BC showed a quick drop from an even higher surface concentration of $23.4 \mu\text{g}/\text{m}^3$ to $8.5 \mu\text{g}/\text{m}^3$ at 246 m. Above 246 m, BC decreased slower from $8.8 \mu\text{g}/\text{m}^3$ at 315 m to $4.5 \mu\text{g}/\text{m}^3$ at 921 m and finally reached a minimum of $1.6 \mu\text{g}/\text{m}^3$ at the top. At 9:00, BC reached $14.8 \mu\text{g}/\text{m}^3$ at the ground level and continued to decrease till 370 m with $1.9 \mu\text{g}/\text{m}^3$. Above this height, BC fluctuated without showing a clear trend compared to the profiles observed at 5:30 and 8:00. Generally, the BC profiles observed in the morning revealed the decrease of BC with height, which was in agreement with most of the previous results (Rahul et al., 2014; Ramana et al., 2010). The shallow mixing layer height in the morning was mainly responsible for the high BC concentrations near the surface. As shown in Fig. 5, the mixing layer height from LST 5:00–9:00 ranged from 150 to 230 m, which was relatively consistent with the turning points of profiles as shown in Fig. 8a when the BC gradient with height became smaller. The continuous near surface emissions from traffic during the morning rush hours and the weak vertical convection shaped the strong BC gradient within the boundary layer. Above the boundary layer, BC was more homogeneously distributed, probably due to the limited intrusion of emissions from below the boundary layer. As discussed above, the BC profile at 09:00 showed a stronger fluctuation than the other two profiles. Although no discernible vertical motion was observed around 9 AM (Fig. 6a), the horizontal wind exhibited an

obvious change from the prevailing northerlies to northwesterlies, especially below 600 m (Fig. 6b). Air masses from the northeast were relatively clean sea breeze compared to the more polluted air masses from inland. In this regard, the change of the horizontal wind direction should be the major cause of the stronger fluctuation of BC profiles measured at 9 AM. Above 600 m, the wind directions are similar throughout the morning hours (Fig. 6b). This explained that the BC concentrations at 9:00 AM at higher altitudes were relatively close to those at 5:30 and 8:00 AM as shown in Fig. 8a. The average BC concentrations within the 1000 m atmospheric column at 5:30, 8:00, and 9:00 were 7.3 , 6.5 , and $4.6 \mu\text{g}/\text{m}^3$, respectively. The lower average BC column concentration after sunrise should be mainly attributed to the change of wind direction. Also, the slightly developed mixing layer height from 150 m at 5:00–230 m at 9:00 also contributed to the decrease of BC to some extent.

3.4.2. Noon and afternoon BC profile

Fig. 8b shows the BC profiles sampled at 12:30, 14:30, and 15:30 during the noon and afternoon phase. At 12:30, BC reached $4.8 \mu\text{g}/\text{m}^3$ near the surface and fluctuated in a narrow range of 4.0 – $4.7 \mu\text{g}/\text{m}^3$ within the height of 204 m–686 m. Above 686 m, stronger fluctuation of BC was observed with the concentration of $5.6 \mu\text{g}/\text{m}^3$ at 741 m, followed by a decrease at 886 m of $3.8 \mu\text{g}/\text{m}^3$ and increased again at 898 m of $6.0 \mu\text{g}/\text{m}^3$. Enhanced BC concentrations were detected, suggesting the presence of BC layers aloft which may derived from the remaining BC particles in the earlier hours. The height 686 m where the turning point occurred was close to the boundary layer top as indicated by Fig. 5. Therefore, the relatively small fluctuation of BC below the height 686 m should be due to the

well mixing within the boundary layer. Above the top of the boundary layer, the turbulence intensified and horizontal winds changed from the prevailing north winds in the morning to a variety of directions (Fig. 6b), hence inducing the significant fluctuation of BC profiles at the higher altitudes. The average BC concentration in the measured total column at 12:30 was $4.6 \mu\text{g}/\text{m}^3$, very close to that of 9:30. From morning to noon, as the day progressed, more entrainment occurred with frequent shift between downward and upward motions. This enhanced convection facilitated the mixing of BC particles and therefore BC concentrations decreased much slower with height.

As for the profile at 14:30, BC showed less fluctuation compared to the profile at 12:30 and it was noted that BC exhibited an increasing tendency starting from 443 m to the top. Surface BC was $4.0 \mu\text{g}/\text{m}^3$ and it increased to $4.6 \mu\text{g}/\text{m}^3$ at the top. As for the BC profile at 15:30, its concentrations were more homogeneously distributed in the range of $3.2\text{--}3.9 \mu\text{g}/\text{m}^3$ within the 1000 m column. The shift between upward and downward vertical convection in the afternoon (Fig. 7a) facilitated a well mixing of the residual BC within the boundary layer. Hence, the dependence of BC on heights was indiscernible.

3.4.3. Early-evening BC profile

Fig. 8c shows the BC profiles at 17:20 and 18:30 in the early-evening phase. At 17:20, the surface concentration of BC was $2.3 \mu\text{g}/\text{m}^3$, and then gradually decreased to $1.2 \mu\text{g}/\text{m}^3$ at 448 m. Above 448 m, there was a pronounced increase of BC to $3.4 \mu\text{g}/\text{m}^3$ at 1000 m. At 18:30, a much more elevated BC concentration of $5.5 \mu\text{g}/\text{m}^3$ was observed near the ground level compared to about 1 h ago. The enhanced traffic emission due to the evening rush hour should be the major cause. A decrease of boundary layer height from 1580 m at 17:00–250 m at 18:30 also contributed to elevation of the near surface BC concentrations. After sunset, sea breeze from the northeast prevailed as shown in Fig. 6b. 24 h backward trajectory at the height of 200 m (Fig. 9a) further indicated the air masses mainly traveled over the ocean but rarely through the inland areas. Hence, this explained a quick decrease of BC from the ground to the height of around 200 m at 18:30. Compared to the profiles in noon and afternoon, the persistent clean sea breeze was mostly responsible for the BC decreases in the height from the ground to around 200 m in the early evening although the Friday traffic congestion was supposed to significantly increase the emissions. Fig. 9b plots the 24 h backward trajectory at the height of 800 m at LST 18:00. Compared to the trajectories at 200 m which dominantly derived from the ocean, a considerable amount of air masses at 800 m travelled through the inland areas, mainly from urban Shanghai and major areas of Jiangsu province where BC emission rates are intense (Fig. S1). Hence, the elevated BC levels in the upper layer should be largely ascribed to the regional transport.

3.4.4. Late-evening BC profile

Fig. 8d shows two BC profiles during the late-evening sampling phase. BC concentrations were $7.1 \mu\text{g}/\text{m}^3$ and $4.9 \mu\text{g}/\text{m}^3$ on the ground level at 20:30 and 23:30, respectively. Above the ground, BC quickly decreased to less than $1 \mu\text{g}/\text{m}^3$ in both profiles at around 160–200 m, which was close to the top of the boundary layer. In the height of around 200–500 m, BC concentrations fluctuated but didn't show clear trends. The average BC concentration within this altitude was $0.82 \pm 0.13 \mu\text{g}/\text{m}^3$ and $0.62 \pm 0.16 \mu\text{g}/\text{m}^3$ at 20:30 and 23:30, respectively. However, above 500 m, BC showed strong enhancements. At 20:30, BC increased from $0.3 \mu\text{g}/\text{m}^3$ at 587 m to $4.3 \mu\text{g}/\text{m}^3$ at 782 m, and then stayed within $3.7\text{--}4.0 \mu\text{g}/\text{m}^3$ till the measured top height. At 23:30, BC showed a quasi-linear increasing trend from $0.7 \mu\text{g}/\text{m}^3$ at 468 m to the maximum of $5.6 \mu\text{g}/\text{m}^3$ at 1000 m. The higher BC concentrations at the upper levels in the late

night should be partly derived from the residual aloft BC layer in the late afternoon. Also, based on the 24-h backward trajectories, air masses shifted from the northeasterlies originating from the East China Sea at lower levels (Fig. 9c) to the westerlies at higher levels (Fig. 9d). The continental flows from the west transported pollutants from inland to the sampling site and should partially account for the higher BC concentrations aloft in the air. The considerable loadings of residual BC in the late evening could be the potential source for the next day as suggested by the measured profiles in the early morning.

3.5. Atmospheric heating rates due to black carbon

Fig. 10 shows the instantaneous heating rates due to black carbon aerosol based on the noon and afternoon profiles. Profiles measured during the morning and evening profiles were not considered either due to the unavailability of meteorology profiles or absence of solar radiation during nighttime. Generally, the vertical profiles of heating rates were as similar as their associated BC profiles. The surface instantaneous heating rate reached 2.75, 1.75, and 1.53 K/day on 12:30, 14:30, and 15:30 PM, respectively. Heating rate at 12:30 showed relatively constant values of $2.75\text{--}3.13 \text{ K/day}$ below 700 m while changed abruptly and reach maximum of more than 4 K/day at the top layer that was measured. As for the profiles at 14:30 and 15:30, heating rates showed more steadily increasing trends with altitudes. At the top layer ($\sim 1000 \text{ m}$), instantaneous heating rates due to black carbon reached 2.74 and 1.85 K/day at 14:30 and 15:30, respectively. The much higher instantaneous heating rate at 12:30 than 14:30 and 15:30 as shown in Fig. 10 was partly due to higher BC concentrations and also due to the lower solar zenith angle. The higher atmospheric heating from black carbon aerosol at the upper layers than the surface would probably induce strengthening of temperature inversion and further lead to poor dispersion. In addition, it was found that the BC stimulated heating caused reduction of the cloud fraction and thus may induce a "cloud burning effect" which may decrease the precipitation (Panicker et al., 2014) and this effect could be more obvious in regard of observation of higher heating rates at higher altitudes where clouds frequently form. Compared to studies of black carbon heating rates in other urban regions (Panicker et al., 2014; Huang et al., 2011; Chakrabarty et al., 2012; Tripathi et al., 2007), this study showed comparable or higher heating rates. It should be noted that the results in this study are derived from a moderately polluted day. The heating effects could be more significant on the monthly average scale during the winter of Shanghai.

4. Conclusions

In December 2013, vertical field measurement of air pollutants and meteorological parameters within the 1000 m lower troposphere was conducted over a Chinese megacity Shanghai for the first time. By using a Tethered balloon filled with 1600 m^3 Helium, a platform was specifically designed to carry monitoring instruments with the maximum payload of 200 kg to ascend and descend at steady speed. Meanwhile, mixing height layer, wind profiles, and the same air pollutants as those measured using the Tethered balloon were synchronously measured on the ground level. On December 13, 2013, ground level BC concentrations were continuously measured with vertical profiles of BC obtained during four different periods. The mean BC concentrations during morning, noon and afternoon, early-evening, and late-evening were 20.0, 5.7, 3.8, and $5.6 \mu\text{g}/\text{m}^3$, respectively. The highest BC level in the morning was partly ascribed to the strong traffic emissions due to the morning rush hours and also due to the very shallow boundary of less than 300 m. Lower BC concentrations during noon, afternoon,

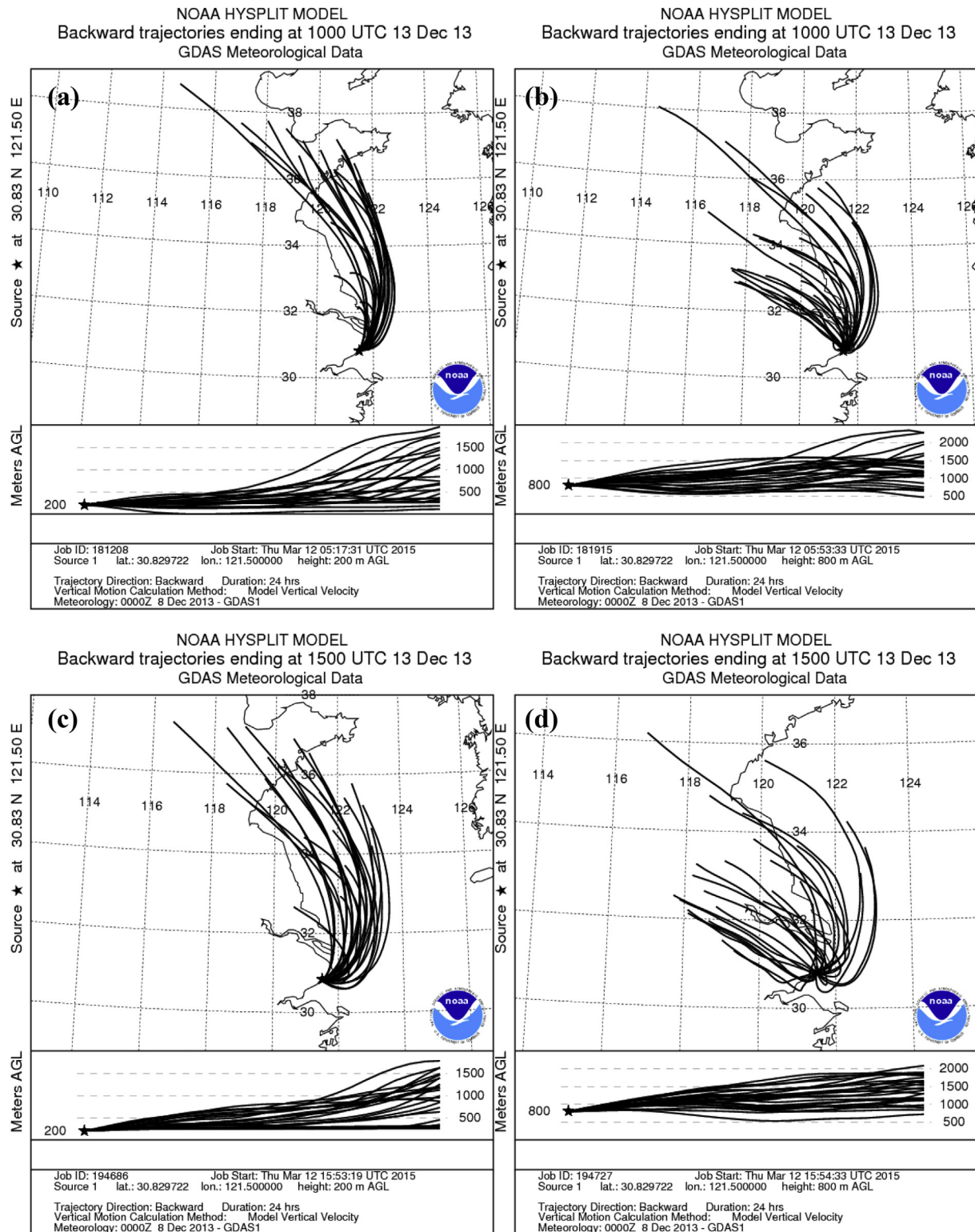


Fig. 9. 24 h backward trajectories starting at (a) LST 18:00 at 200 m, (b) LST 18:00 at 800 m, (c) LST 23:00 at 200 m, and (d) LST 23:00 at 800 m.

and early-evening were attributed to the decreased source emissions and relatively favorable synoptic weather conditions, e.g. extended mixing layer height, change of wind direction from inland to ocean, and intensified vertical turbulence.

The morning BC profile exhibited strong gradients with altitudes from the ground to the top of boundary layer at around

250–370 m. The majority of BC loading was confined within this shallow boundary layer. Above the boundary layer, the BC gradients were much smaller due to the limited intrusion of emissions from below the boundary layer. BC profiles measured during noon and afternoon were more homogeneously distributed with heights. The largely extended boundary layer due to enhanced solar radiation

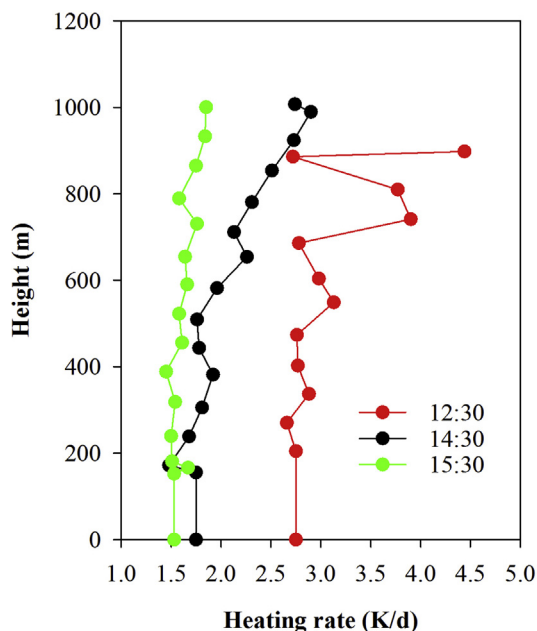


Fig. 10. The instantaneous heating rates (K/d) due to black carbon aerosol based on the profiles measured at 12:30 (solar zenith angle θ of 55°), 14:30 (θ of 69°), and 15:30 (θ of 74°), respectively.

and intensified vertical convection accounted for this well mixing of BC particles. BC profiles measured in the early-evening and late-evening phases were similar to some extent. Two stratified air layers were formed with contrasted BC vertical distributions in the lower troposphere. All profiles at night showed strong gradients from the relatively high surface concentrations to low concentrations near the top of the boundary layer around 200 m. Backward trajectories at 200 m indicated air parcels travelled over the Eastern China Sea, thus quickly cleansing the pollutants within the boundary layer. Oppositely, BC concentrations presented evident increases with altitudes from around 500–600 m and reached a maximum at the top of 1000 m. Backward trajectories at 800 m suggested considerable air parcels from the inland populous areas, indicating that the addition of regional transport with local emissions was responsible for the elevated BC concentrations aloft. The instantaneous heating rates due to black carbon aerosol were simulated by a radiative transfer model. It is calculated that heating rates near the surface reached 2.75, 1.75, and 1.53 K/day on 12:30, 14:30, and 15:30 PM, respectively. Higher atmospheric heating due to black carbon aerosol at the upper layers than the surface would probably induce strengthening of temperature inversion and further lead to poor dispersion, as well as affecting the formation of clouds and precipitation.

As the first study on aerosol vertical distribution over Eastern China using a Tethered balloon, the vertical distribution of BC was revealed over a region with the most intense BC emission rates in China. The detailed BC profiles obtained in this study will greatly advance the improvement of numerical simulation (e.g. plume rise module) applied in the Chinese urban areas in the future study. As the second largest contributor to global warming only inferior to carbon dioxide, this study also has profound implications for more accurately assessing the climatic effects on the regional scale.

Acknowledgment

The research was financially sponsored by Shanghai Municipal Commission of Economy and Informatization (No. 201202028),

Scientific Project of Shanghai Environmental Protection Bureau (No. 2012-01 and No. 2014-8), and Youth Fund Project of Shanghai Environmental Protection Bureau (No. 2013-63). Dr. Kan Huang is partially supported by National Natural Science Foundation of China (Grant No. 41429501, fund for collaboration with overseas scholars) and Environmental charity project of Ministry of Environmental Protection of China (201409022). The authors are very grateful for the great support of Fahe Chai from Chinese Research Academy of Environmental Science. Dongnian Fei serving at No. 38 institute of China Electronics Technology Group Company made a great contribution in the field measurements. Also, we would like to thank Weili Lin, Xinqin An from Chinese Meteorological Administration as well as Zhiqiang Ma from Beijing Meteorological Bureau for their input in the harsh campaign.

Appendix A. Supplementary data

Supplementary data related to this article can be found at <http://dx.doi.org/10.1016/j.atmosenv.2015.08.096>.

References

- Arnott, W.P., Hamasha, K., Moosmuller, H., Sheridan, P.J., Ogren, J.A., 2005. Towards aerosol light-absorption measurements with a 7-wavelength aethalometer: evaluation with a photoacoustic instrument and 3-wavelength nephelometer. *Aerosol Sci. Technol.* 39 (1), 17–29.
- Babu, S.S., Moorthy, K.K., Manchanda, R.K., Sinha, P.R., Satheesh, S.K., Vajja, D.P., Srinivasan, S., Kumar, V.H.A., 2011. Free tropospheric black carbon aerosol measurements using high altitude balloon: do BC layers build “their own homes” up in the atmosphere? *Geophys. Res. Lett.* 38.
- Baumbach, G., Baumann, K., Grauer, A., Semmler, R., Streisslinger, B., Wanner, H., Kuenzle, Th, Neu, U., 1993. A tethered sonde measuring system for detection of O₃, NO₂, hydrocarbon concentrations, and meteorological parameters in the lower boundary layer. *Meteorol. Z.* 3, 178–188.
- Chakrabarty, R.K., Garro, M.A., Wilcox, E.M., Moosmuller, H., 2012. Strong radiative heating due to wintertime black carbon aerosols in the Brahmaputra River Valley. *Geophys. Res. Lett.* 39.
- Chan, C.K., Yao, X., 2008. Air pollution in mega cities in China. *Atmos. Environ.* 42, 1–42.
- Chen, C., Huang, C., Jing, Q., Wang, H., Pan, H., Li, L., Zhao, J., Dai, Y., Huang, H., Schipper, L., Streets, D.G., 2007. On-road emission characteristics of heavy-duty diesel vehicles in Shanghai. *Atmos. Environ.* 41, 5334–5344.
- Chou, M.D., Suarez, M.J., 1999. A shortwave radiation parameterization for atmospheric studies. In: *Technical Report Series on Global Modeling and Data Assimilation*, vol. 15. NASA/TM-1999-104606. 40 pp.
- Chou, M.D., Chan, P.K., Wang, M., 2002. Aerosol radiative forcing derived from SeaWiFS-Retrieved aerosol optical properties. *J. Atmos. Sci.* 59, 748–757.
- Chow, J.C., Watson, J.G., Lowenthal, D.H., Antony Chen, L.W., Motallebi, N., 2011. PM_{2.5} source profiles for black and organic carbon emission inventories. *Atmos. Environ.* 45 (31), 5407–5414.
- Cuchiara, G.C., Li, X., Carvalho, J., Rappengluck, B., 2014. Intercomparison of planetary boundary layer parameterization and its impacts on surface ozone concentration in the WRF/Chem model for a case study in Houston/Texas. *Atmos. Environ.* 96, 175–185.
- D’Amato, G., Baena-Cagnani, C.E., Cecchi, L., Annesi-Maesano, I., Nunes, C., Ansoategui, I., D’Amato, M., Liccardi, G., Sofia, M., Canonica, W.G., 2013. Climate change, air pollution and extreme events leading to increasing prevalence of allergic respiratory diseases. *Multidiscip. Resp. Med.* 8.
- Day, B.M., Rappengluck, B., Clements, C.B., Tucker, S.C., Brewer, W.A., 2010. Nocturnal boundary layer characteristics and land breeze development in Houston, Texas during TexAQS II. *Atmos. Environ.* 44, 4014–4023.
- Ding, A.J., Wang, T., Xue, L.K., Gao, J., Stohl, A., Lei, H.C., Jin, D.Z., Ren, Y., Wang, X.Z., Wei, X.L., Qi, Y.B., Liu, J., Zhang, X.Q., 2009. Transport of north China air pollution by midlatitude cyclones: case study of aircraft measurements in summer 2007. *J. Geophys. Res.* 114.
- Dupont, E., Menut, L., Carissimo, B., Pelon, J., Flamant, P., 1999. Comparison between the atmospheric boundary layer in Paris and its rural suburbs during the ECLAP experiment. *Atmos. Environ.* 33, 979–994.
- Emeis, S., Schäfer, K., Münkel, C., 2008. Surface-based remote sensing of the mixing-layer height – a review. *Meteorol. Z.* 17, 621–630.
- Eresmaa, N., Karppinen, A., Joffre, S.M., Rasanen, J., Talvitie, H., 2006. Mixing height determination by ceilometer. *Atmos. Chem. Phys.* 6, 1485–1493.
- Fomin, B.A., Correa, M.P., 2005. A k-distribution technique for radiative transfer simulation in inhomogeneous atmosphere: 2. FKDM, fast k-distribution model for the shortwave. *J. Geophys. Res.* 110, D02106. <http://dx.doi.org/10.1029/2004JD005163>.
- Geng, F.H., Zhang, Q., Tie, X.X., Huang, M.Y., Ma, X.C., Deng, Z.Z., Yu, Q., Quan, J.N., Zhao, C.S., 2009. Aircraft measurements of O₃, NO_x, CO, VOCs, and SO₂ in the

- Yangtze River Delta region. *Atmos. Environ.* 43, 584–593.
- Greenberg, J.P., Guenther, A.B., Turnipseed, A., 2009. Tethered balloon-based soundings of ozone, aerosols, and solar radiation near Mexico City during MIRAGE-MEX. *Atmos. Environ.* 43, 2672–2677.
- Hand, E., 2014. China blamed for US ozone. *Science* 345, 1233–1233.
- Hao, J., He, K., Duan, L., Li, J., Wang, L., 2007. Air pollution and its control in China. *Front. Environ. Sci. Eng. China* 1, 129–142.
- Huang, X.F., Gao, R.S., Schwarz, J.P., He, L.Y., Fahey, D.W., Watts, L.A., McComiskey, A., Cooper, O.R., Sun, T.L., Zeng, L.W., Hu, M., Zhang, Y.H., 2011. Black carbon measurements in the Pearl River Delta region of China. *J. Geophys. Res. Atmos.* 116.
- Huang, K., Zhuang, G., Lin, Y., Wang, Q., Fu, J.S., Zhang, R., Li, J., Deng, C., Fu, Q., 2012. Impact of anthropogenic emission on air quality over a megacity – revealed from an intensive atmospheric campaign during the Chinese Spring Festival. *Atmos. Chem. Phys.* 12 (23), 11631–11645.
- Jacob, D.J., Winner, D.A., 2009. Effect of climate change on air quality. *Atmos. Environ.* 43, 51–63.
- Ji, D., Li, L., Wang, Y., Zhang, J., Cheng, M., Sun, Y., Liu, Z., Wang, L., Tang, G., Hu, B., Chao, N., Wen, T., Miao, H., 2014. The heaviest particulate air-pollution episodes occurred in northern China in January, 2013: insights gained from observation. *Atmos. Environ.* 92, 546–556.
- Johnson, B.J., Helmig, D., Oltmans, S.J., 2008. Evaluation of ozone measurements from a tethered balloon-sampling platform at South Pole Station in December 2003. *Atmos. Environ.* 42, 2780–2787.
- Kan, H.D., Chen, R.J., Tong, S.L., 2012. Ambient air pollution, climate change, and population health in China. *Environ. Int.* 42, 10–19.
- Knapp, K.G., Jensen, M.L., Balslev, B.B., Bogner, J.A., Oltmans, S.J., Smith, T.W., Birks, J.W., 1998. Vertical profiling using a complementary kite and tethered balloon platform at Ferryland Downs, Newfoundland, Canada: observation of a dry, ozone-rich plume in the free troposphere. *J. Geophys. Res. Atmos.* 103, 13389–13397.
- Lin, C.H., Lai, C.H., Wu, Y.L., Lai, H.C., Lin, P.H., 2007. Vertical ozone distributions observed using tethered ozonesondes in a coastal industrial city, Kaohsiung, in southern Taiwan. *Environ. Monit. Assess.* 127, 253–270.
- Lin, J., Pan, D., Davis, S.J., Zhang, Q., He, K., Wang, C., Streets, D.G., Wuebbles, D.J., Guan, D., 2014. China's international trade and air pollution in the United States. *Proc. Natl. Acad. Sci.* 111, 1736–1741.
- Liu, X., Zhang, Y., Han, W., Tang, A., Shen, J., Cui, Z., Vitousek, P., Erisman, J.W., Goulding, K., Christie, P., Fangmeier, A., Zhang, F., 2013. Enhanced nitrogen deposition over China. *Nature* 494, 459–462.
- Ma, Z.Q., Xu, H.H., Meng, W., Zhang, X.L., Xu, J., Liu, Q., Wang, Y.S., 2013. Vertical ozone characteristics in urban boundary layer in Beijing. *Environ. Monit. Assess.* 185, 5449–5460.
- Meng, Z.Y., Ding, G.A., Xu, X.B., Xu, X.D., Yu, H.Q., Wang, S.F., 2008. Vertical distributions of SO₂ and NO₂ in the lower atmosphere in Beijing urban areas, China. *Sci. Total Environ.* 390, 456–465.
- Ni, T., Han, B., Bai, Z., 2012. Source apportionment of PM10 in four cities of north-eastern China. *Aerosol Air Qual. Res.* 12, 571–582.
- Ouyang, Y., 2013. China wakes up to the crisis of air pollution. *Lancet Respir. Med.* 1, 12.
- Panicker, A.S., Pandithurai, G., Safai, P.D., Dipu, S., Prabha, T.V., Konwar, M., 2014. Observations of black carbon induced semi direct effect over Northeast India. *Atmos. Environ.* 98, 685–692.
- Park, R.J., Jacob, D.J., Field, B.D., Yantosca, R.M., Chin, M., 2004. Natural and trans-boundary pollution influences on sulfate-nitrate-ammonium aerosols in the United States: implications for policy. *J. Geophys. Res. Atmos.* 109, D15204.
- Rahul, P.R.C., Bhawar, R.L., Ayantika, D.C., Panicker, A.S., Safai, P.D., Tharaprabhakaran, V., Padmakumari, B., Raju, M.P., 2014. Double blanket effect caused by two layers of black carbon aerosols escalates warming in the Brahmaputra River Valley. *Sci. Rep.* 4.
- Ramana, M.V., Ramanathan, V., Feng, Y., Yoon, S.C., Kim, S.W., Carmichael, G.R., Schauer, J.J., 2010. Warming influenced by the ratio of black carbon to sulphate and the black-carbon source. *Nat. Geosci.* 3, 542–545.
- Ramanathan, V., Carmichael, G., 2008. Global and regional climate changes due to black carbon. *Nat. Geosci.* 1, 221–227.
- Rappengluck, B., Forster, C., Jakobi, G., Pesch, M., 2004. Unusually high levels of PAN and ozone over Berlin, Germany, during nighttime on August 7, 1998. *Atmos. Environ.* 38, 6125–6134.
- Smith, K.R., Jerrett, M., Anderson, H.R., Burnett, R.T., Stone, V., Derwent, R., Atkinson, R.W., Cohen, A., Shonkoff, S.B., Krewski, D., Pope III, C.A., Thun, M.J., Thurston, G., 2009. Public health benefits of strategies to reduce greenhouse-gas emissions: health implications of short-lived greenhouse pollutants. *Lancet* 374, 2091–2103.
- Tagaris, E., Liao, K.J., Delucia, A.J., Deck, L., Amar, P., Russell, A.G., 2009. Potential impact of climate change on air pollution-related human health effects. *Environ. Sci. Technol.* 43, 4979–4988.
- Tai, A.P.K., Martin, M.V., Heald, C.L., 2014. Threat to future global food security from climate change and ozone air pollution. *Nat. Clim. Change* 4, 817–821.
- Tripathi, S.N., Srivastava, A.B.K., Dey, S., Satheesh, S.K., Krishnamoorthy, K., 2007. The vertical profile of atmospheric heating rate of black carbon aerosols at Kanpur in northern India. *Atmos. Environ.* 41, 6909–6915.
- Wang, S.-H., Lin, N.-H., Chou, M.-D., Woo, J.-H., 2007. Estimate of radiative forcing of Asian biomass-burning aerosols during the period of TRACE-P. *J. Geophys. Res.* 112, D10222. <http://dx.doi.org/10.1029/2006JD007564>.
- Wang, L.T., Wei, Z., Yang, J., Zhang, Y., Zhang, F.F., Su, J., Meng, C.C., Zhang, Q., 2014. The 2013 severe haze over southern Hebei, China: model evaluation, source apportionment, and policy implications. *Atmos. Chem. Phys.* 14, 3151–3173.
- Winkler, J., Blank, P., Glaser, K., Gomes, J.A.G., Habram, M., Jambert, C., Jaeschke, W., Konrad, S., Kurtenbach, R., Lenschow, P., Lorz, J.C., Perros, P.E., Pesch, M., Prumke, H.J., Rappengluck, B., Schmitz, T., Slemr, F., Volz-Thomas, A., Wickert, B., 2002. Ground-based and airborne measurements of nonmethane hydrocarbons in BERLIOZ: analysis and selected results. *J. Atmos. Chem.* 42, 465–492.
- Xu, P., Chen, Y., Ye, X., 2013. Haze, air pollution, and health in China. *Lancet* 382, 2067–2067.
- Xue, L.K., Ding, A.J., Gao, J., Wang, T., Wang, W.X., Wang, X.Z., Lei, H.C., Jin, D.Z., Qi, Y.B., 2010. Aircraft measurements of the vertical distribution of sulfur dioxide and aerosol scattering coefficient in China. *Atmos. Environ.* 44, 278–282.
- Yamazaki, S., Shima, M., Yoda, Y., Oka, K., Kurosaka, F., Shimizu, S., Takahashi, H., Nakatani, Y., Nishikawa, J., Fujiwara, K., Mizumori, Y., Mogami, A., Yamada, T., Yamamoto, N., 2014. Association between PM2.5 and primary care visits due to asthma attack in Japan: relation to Beijing's air pollution episode in January 2013. *Environ. Health Prev.* 19, 172–176.
- Yerramilli, A., Challa, V.S., Indracanti, J., Dasari, H., Baham, J., Patrick, C., Young, J., Hughes, R., White, L.D., Hardy, M.G., Swanier, S., 2008. Some observational and modeling studies of the atmospheric boundary layer at Mississippi Gulf Coast for air pollution dispersion assessment. *Int. J. Environ. Res. Public Health* 5, 484–497.
- Zhang, X.Y., Wang, Y.Q., Niu, T., Zhang, X.C., Gong, S.L., Zhang, Y.M., Sun, J.Y., 2012. Atmospheric aerosol compositions in China: spatial/temporal variability, chemical signature, regional haze distribution and comparisons with global aerosols. *Atmos. Chem. Phys.* 12, 779–799.